

New Magnetic Resonance Approaches for Assessing Structure and Strength of Trabecular Bone

Felix W. Wehrli, Ph.D.
University of Pennsylvania Medical Center,
Philadelphia, Pennsylvania, USA

Introduction

Bone is a composite material consisting of an inorganic phase ... calcium apatite $\text{Ca}_{10}(\text{PO}_4)_6(\text{OH})_2$ corresponding to about 65 % of total volume ... and an organic phase, essentially collagen, accounting for most of the remaining 35 %. From an architectural point of view bone can be subdivided into cortical and trabecular, the latter providing for most of the strength of the axial skeleton (e.g., the vertebral column) and the portions of the appendicular skeleton near the joints. Trabecular bone is made up of a three-dimensional network of struts and plates, the trabeculae, which are on the order of 100–150 μm in width spaced 300–1000 μm apart.

Like engineering materials, trabecular bone derives its mechanical strength from its inherent elastic properties, its volume density, and its structural arrangement. Bone is constantly renewed through a hormonally regulated process called "bone remodeling", a term referring to a dynamic equilibrium between bone formation and bone resorption, controlled by two essential types of cells: the osteoblasts ... bone forming cells ... and the osteoclasts, bone resorbing cells. During bone formation, osteoblasts eventually become imbedded in bone, turning into osteocytes, which presumably act as piezoelectric sensors transmitting signals to the osteoblasts to induce bone formation. Since the seminal work by Wolff (1) it is known that bone grows in response to the forces to which it is subjected. Therefore, weightlessness and physical inactivity are well known factors inducing bone loss.

The most common pathologic process in which bone mineral homeostasis is perturbed is osteoporosis (2). Among the various etiologies, post-menopausal osteoporosis, which results from increased osteoclast activity, is the most frequent form of the disease, afflicting a substantial fraction of the elderly female population. The most common clinical manifestations are fractures of the hip and vertebrae. If detected early, calcium supplements and estrogen replacement are effective forms of therapeutic intervention. Further, the development of drugs inhibiting osteoclastic

activity, is in progress and some are already available. In addition, therapeutic analogs of cortisol can have dramatic effects on mineral homeostasis, causing rapid bone loss and morbidity (3, 4). This form of osteoporosis, though reversible to some extent, is widespread due to the common treatment of inflammatory conditions with corticosteroids.

Bone mineral density is the most widely invoked criterion for fracture risk assessment, typically measured by dual x-ray absorptiometry (DEXA), which is based on the measurement of the attenuation coefficient in a quantitative radiographic procedure, or by quantitative computed tomography (QCT). Whereas both methods measure bone mineral density with sufficient precision, neither provides information on the properties or structural arrangement of the bone. NMR, on the other hand, has the potential to probe structure as well as chemical composition of bone, both relevant to biomechanical competence.

Direct Detection of Bone Mineral by ^{31}P NMR

The difficulties of detecting phosphorus in the solid state *in vivo* are considerable but do not seem insurmountable. The problems are symptomatic of high-resolution NMR in the solid state in general: a combination of long T_1 (on the order of minutes) and short T_2 (on the order of 100 μs), as well as additional line broadening by anisotropic chemical shift and dipolar coupling.

Brown et al first demonstrated the feasibility of quantitative analysis by solid-state ^{31}P spectroscopy in human limbs as a means of measuring bone mineral density noninvasively (5). Imaging adds an additional level of complexity since the short lifetime of the signal demands short gradient duration, a requirement which can only be reconciled with gradients of high amplitude and large slew rates, both difficult to achieve in large sample volumes. Ackerman et al (6) produced one-dimensional spin-echo images at 7.4T with echo times on the order of 1 ms and flip-back 180° RF pulses as a means to restore the longitudinal magnetization, inverted by the phase-reversal pulse. More recently, the same group of workers reported two-dimensional images of chicken bone at 6T by means of a combination of back-projection and ^1H - ^{31}P cross polarization for sensitivity enhancement, with echo times as short as 200 μs (7). In the cross polarization technique the ^{31}P magnetization is derived from that of dipolar-coupled protons which have shorter T_1 and thus permit shorter pulse sequence recycling times. Making use of the dependence of the cross polarization rate on the proton - phosphorus dipolar coupling, the same laboratory showed that different phosphate species can be distinguished demonstrating the presence of a minor HPO_4^{2-} species in immature chicken bone (8). While this work is at an early stage, it clearly has unique potential for nondestructive assaying of the chemical composition and its age-related

changes of bone, parameters that might in part explain the increased fragility of bone in older individuals.

Induced Magnetic Fields and their Implications on Transverse Relaxation

Another approach toward assessing the properties of trabecular bone ... specifically as its architectural arrangement is concerned ... exploits the diamagnetic properties of bone mineral. By virtue of the higher atomic number of its elemental composition (i.e., calcium and phosphorus), mineralized bone is more diamagnetic than marrow constituents in the trabecular marrow cavities, which consist mainly of water and lipids (i.e., oxygen, carbon and hydrogen).

It is well known that near the interface of two materials of different magnetic susceptibility, and depending on the geometry of the interface, the magnetic field is inhomogeneous. Among the first to investigate these effects systematically, were Glasel and Lee (9) who studied deuteron relaxation of beads of different size and susceptibility, suspended in $^2\text{H}_2\text{O}$. Specifically, they showed that the line width, $1/\pi T_2^*$, scaled with $\Delta\chi$, the difference in volume susceptibility between the beads and deuterium oxide. The transverse relaxation rate, $1/T_2$, was found to increase linearly with reciprocal bead size, and observation which could be reconciled with diffusion in the induced magnetic field gradients. Similar phenomena were reported by Davis et al (10), who measured proton NMR line widths at 5.9 T in powdered bone suspended in various solvents and found T_2^* to decrease with decreasing grain size and thus increased surface-to-volume ratio.

One of the earliest studied magnetically heterogeneous systems in biology is lung tissue where the local magnetic field distortions are caused by air in the alveoli, and some of the concepts described here have parallels in imaging pulmonary parenchyma (11). Transverse relaxation enhancement from diffusion in intrinsic microscopic gradients has recently received increased attention in conjunction with the BOLD contrast phenomenon, resulting from physiologic variations of deoxyhemoglobin in capillary vessels during functional activation (12, 13). However, since trabeculae are considerably larger than the capillaries (100–200 μm versus 10–20 μm) and diffusion of the protons in the marrow spaces is small ($\sim 10^{-5}$ cm^2/s), diffusion-induced shortening of T_2 is expected to be negligible (14). Consequently, the effect of the susceptibility-induced inhomogeneous field is essentially line broadening.

Suppose a distribution $\Delta H(x,y,z)$ across the sample volume such as an imaging voxel of dimension $\Delta x\Delta y\Delta z$, then the transverse magnetization $M_{xy}(t)$ can be written as:

$$M_{x,y}(t) = \frac{M_0}{\Delta x \Delta y \Delta z} e^{-t/T_2} \int_{\Delta x} \int_{\Delta y} \int_{\Delta z} e^{i\gamma \Delta H(x,y,z)t} dx dy dz \quad (1)$$

For a Lorentzian field distribution the integral of eq. (1) can be described as an additional damping term, yielding

$$M_{x,y}(t) = M_0 e^{-t/T_2} e^{-t/T_2^*} \quad (2)$$

In eq. (2) T_2^* thus is the time constant for inhomogeneity-induced spin dephasing¹. While the line broadening in general, of course, may not Lorentzian (14-16), it will be seen subsequently that the assumption of a single exponential time constant is often a valid approximation.

Susceptibility of Bone

Until recently, the susceptibility of trabecular bone has been controversial. Ford et al. (17) estimated a value of -1.02 ppm (CGS), thus suggesting bone to be considerably more diamagnetic than water. By contrast, Sumanaweera and Glover (18), using SQUID techniques, found a value of -0.71 ppm, implying the bone's susceptibility to be almost equal to that of water, -0.719 ppm. More recent preliminary work by Hwang et al. (19) and Chung et al (20), on the basis of the induced phase shift in images of trabecular bone, imply bone to be more diamagnetic than water by at least 0.2 ppm, thus suggesting a susceptibility on the order -0.9 to -1.0 ppm.

¹ In the following the subsequent definitions and notations shall be used for the contribution from magnetic field inhomogeneity to the total dephasing rate, $1/T_2^*$, irrespective of the notation in the original literature:

$$1/T_2^* \equiv R_2' \approx \frac{\gamma \Delta H_z}{2} = 1/T_2^* - 1/T_2$$

with ΔH_z representing the full width at half maximum of the magnetic field histogram in the sampling volume such as the imaging voxel.

Based on earlier experiments by the author (21) Hopkins and Wehrli (22) determined the absolute susceptibility of bone using a susceptibility matching technique (23). For this purpose, powdered bone from bovine ribs was suspended in a cylindrical sample tube with a coaxial capillary containing water and serving as a reference, both aligned along the axis of a superconducting magnet and (diamagnetic) potassium chloride, added incrementally to the suspension. This operation resulted in a decrease in line width and increase in the bulk magnetic susceptibility (BMS) shift. The spectroscopic linewidth of the KCl solution is governed by the susceptibility by bulk magnetic susceptibility induced frequency shifts in the fluid resonance. Correlating the two dependencies allowed measurement of the absolute volume susceptibility of the solid. The susceptibility of bovine rib bone was found to be $-0.90 \pm 0.02 \times 10^{-6}$ (CGS) confirming previous estimates which suggested bone to be more diamagnetic than the marrow constituents.

Theoretical Considerations, Computer Modeling and Experimental Verification

Let us now briefly review the susceptibility-induced magnetic field from first principles of magnetostatics. For this purpose consider two adjoining materials of susceptibility χ_m and χ_b . The induced magnetic surface charge density σ at some location on the interface between the two materials then is given as:

$$\sigma = \Delta\chi H_o n \tag{3}$$

In eq. (4) \mathbf{n} is the unit vector normal to the interface and $\Delta\chi = \chi_m - \chi_b$. The additional field $H_i(r)$ resulting from the magnetic charges at the phase boundary can be estimated from the Coulomb integral (eq. (5)) (24):

$$H_i(r) = \int \sigma(r') \frac{r - r'}{|r - r'|^3} dS' \tag{4}$$

with integration running over the surface S of the interface, with r' and r representing the location of the source H and field point, respectively.

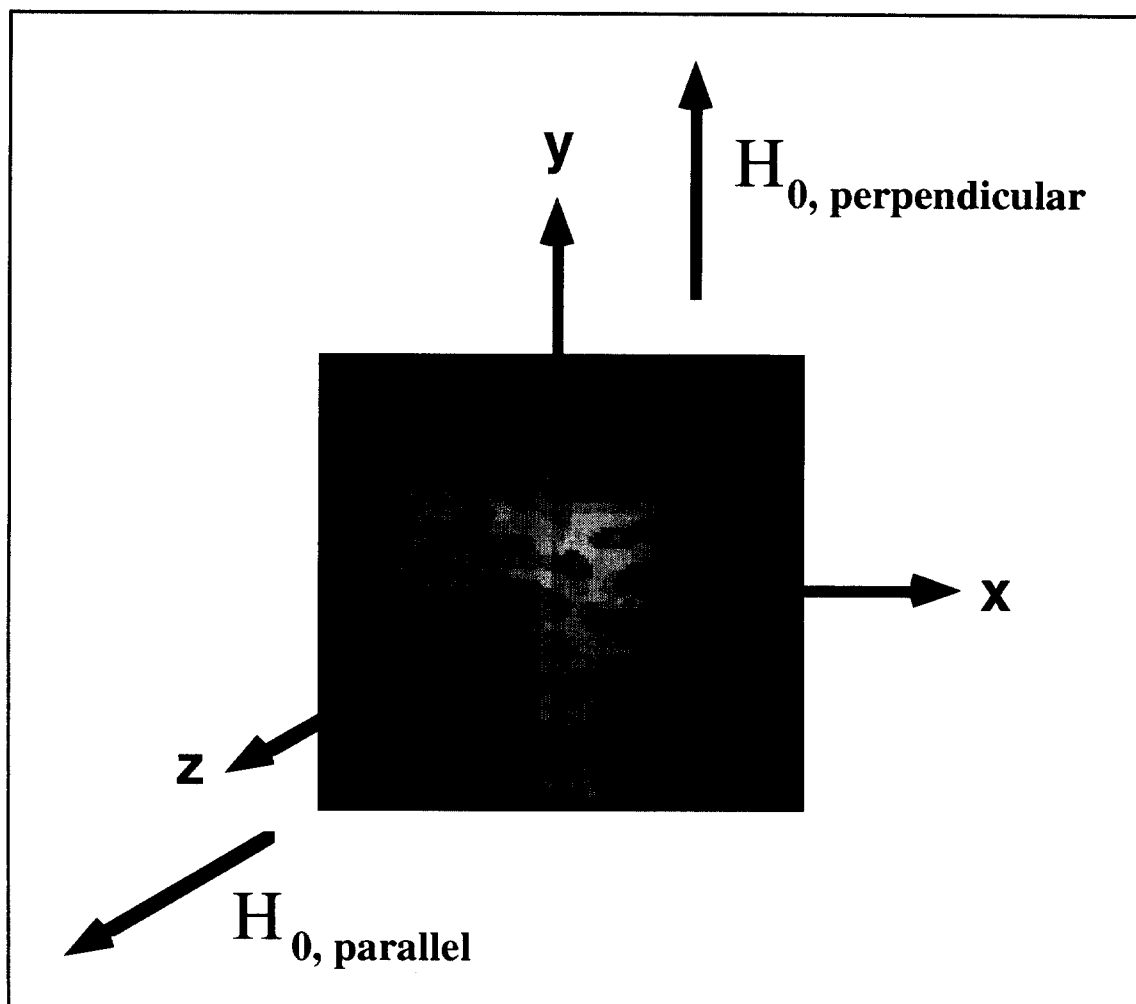
The induced field thus is proportional to the difference in susceptibility of the two adjoining materials, the strength of the applied field and the inverse square of the distance between source and field location. For an array of trabeculae the field should be highly inhomogeneous and a

relationship is expected to exist between the magnetic field distribution within the volume of interest, and the number density, thickness and orientation of trabeculae.

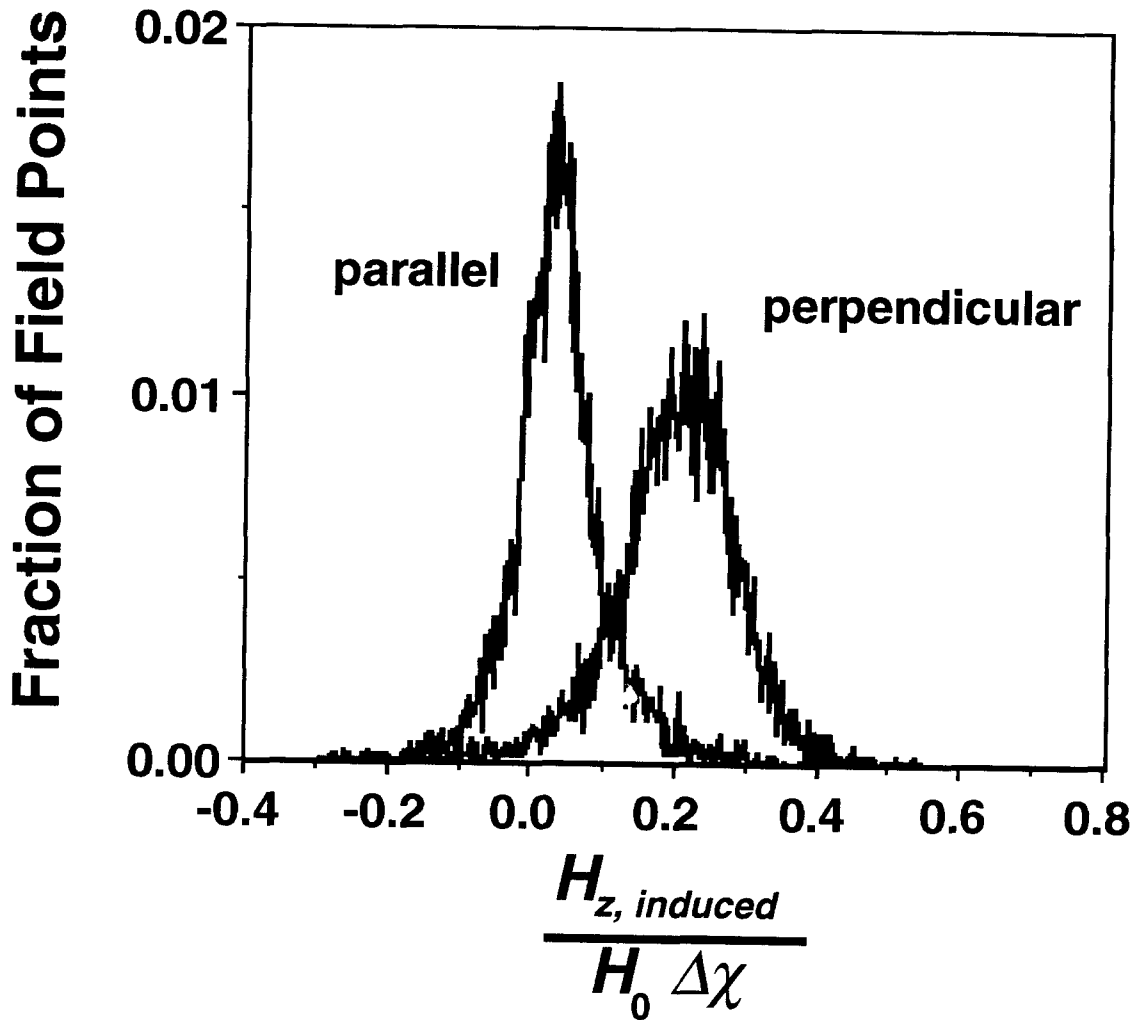
Ford et al. (17) invoked a three-dimensional model that resembles strut-like trabecular bone as it is found in the vertebrae (25), to predict the line broadening behavior of protons in the marrow spaces, as a means to investigate the structural dependence of R_2' . The model consists of a tetragonal lattice of interconnected parallelepipeds ('struts') of square cross section differing in their susceptibility from that of the medium by $\Delta\chi$. When oriented so that the two parallel faces of each transverse strut area normal to the direction of the applied field H_0 then, according to eq. (3), these two faces will have uniform charge density $\sigma = \pm \Delta\chi H_0$. The other faces of the transverse (and longitudinal) struts will have $\sigma = 0$, and thus do not contribute to $H_i(r)$. If the field is oriented arbitrarily relative to the lattice, all faces will be uniformly polarized with a charge density $\sigma = \Delta\chi H_0 \cos\alpha$ where α represents the angle between H_0 and the unit vector normal to any given polarized surface. An analytical expression exists for the induced field given by the integral of eq. (4) for a rectangular lamina and thus the total field at any one point in space can be calculated as a sum of contributions from all charge-bearing faces. In this manner, a histogram of the field for the unit cell of this lattice was obtained by randomly placing field points within the unit cell, and R_2 calculated by fitting the Fourier transform of the field histogram to a decaying exponential. The model predicts nearly exponential decay within the range of echo times experimentally practical (ca. 10–50 ms). Further, R_2 is predicted to increase with both the number density of transverse struts, as well as their thickness. Since the latter two quantities scale with material density, this finding appears unremarkable as it would imply that R_2 merely measures bone mineral density. However, if both strut thickness and number density are varied in an apposite manner (so as to keep material density constant), the model indicates R_2 to increase as strut thickness decreases and number density increases. These predictions, which have been confirmed in analogous physical models (26), underscore the importance of the distribution of the material and suggest that different etiologies of bone loss (e.g., trabecular thinning as opposed to loss of trabecular elements) might be distinguishable.

Hwang and Wehrli (27) computed the magnetic field distribution in trabecular bone of human and bovine origin on the basis of a surface model derived from isotropic 3D high-resolution images. Surfaces were modeled with triangular elements of constant magnetic surface charge density. The induced field was then computed from the charged triangles using a hierarchical multipole algorithm. Validation of the technique on a spherical object showed excellent agreement with the analytical solution. The method was applied to computing histograms of the induced fields

in specimens of trabecular bone. A 76x76x76 array of image voxels resulted in 322,169 triangles and required 70 minutes computation time for evaluating the field at 100,000 locations on a Sun Sparc 10 workstation. The width of the induced field distributions was found to be narrowest when the polarizing field was parallel to the preferred orientation of the trabeculae, confirming previous experimental findings (28) and thus demonstrating the anisotropic nature of the effect. **Fig. 1** shows a histogram of the induced magnetic field, derived from 3D magnetic resonance micrograms of bovine tibia with the magnetic field oriented along with cross-sectional images.



(a)



(b)

Figure 1. Induced magnetic field in trabecular bone from bovine tibia: (a) Shaded 3D surface display derived from 3D NMR micrograms. (b) histogram of the induced magnetic field resulting from the bone's diamagnetism with respect to the marrow constituents.

The dependence of the induced field, expressed in terms of the reversible contribution to the effective transverse relaxation rate, R_2' , was investigated by Yablonskiy and Haacke (14), who derived an analytical solution for R_2' in a model of trabecular bone consisting of a regular distribution of cylindrical columns and struts. They showed that beyond a critical time within which signal decay is Gaussian, signal evolution can be described by a single exponential time constant

$$R_2' \propto \Delta \chi B_o \left[\zeta_h + \left(\zeta_v - \frac{1}{2} \zeta_h \right) \sin^2 \theta \right] \quad (5)$$

where $\Delta \chi$ is the susceptibility difference between bone and marrow, ζ_h and ζ_v are bone densities of the struts and columns, respectively, and θ is the angle between the magnetic field B_o and the columns. Yablonskiy et al. demonstrated the angular dependence of R_2' in a simple trabecular bone phantom composed of parallel polyethylene filaments (29) and found their experimental findings to agree well with their theory. Similar findings were reported by Selby *et al* (30) in microphantoms consisting of cylindrical Pyrex rods. Previously Chung et al. (28) had demonstrated the anisotropic behavior of the effective transverse relaxation time, R_2' , in vivo in the distal radius where trabeculae are highly ordered, following the anatomic axis. This finding was confirmed by Yablonskiy et al. (29) who found R_2' in the radius to be twice as large with the axis of the wrist perpendicular to the direction of the field.

As implied by eq. (3) the magnetic charge density to which the induced magnetic field is proportional, scales with magnetic field strength. Therefore one would expect a linear relationship between trabecular bone marrow R_2' and field strength. Parizel *et al.* (31) reported the field strength dependence of R_2' from measurement of gradient echo signal decay at 1.5, 1.0 and 0.2T in vertebral bone marrow in a single volunteer. More recently,, Song et al. (32, 33) performed a detailed study of the field strength dependence of R_2 and R_2' in the calcaneus at 1.5T and 4T by means of the GESFIDE technique described below (34). They found R_2' to scale nearly proportionally with field strength while R_2 was almost field strength invariant. The data, which show that at 4T R_2' accounts for nearly 90 % of the total relaxation rate ($R_2 = R_2 + R_2'$), are summarized in Table 1.

Table 1. Bone marrow relaxation rates and standard deviations in the calcaneus in s^{-1} ($n=5$). $R_2'(4T)/R_2'(1.5T) = 2.73$. The rates were measured from a rectangular ROI encompassing most of the calcaneus with the sole of the foot perpendicular to the direction of the main field. Standard deviations represent variations among the five subjects (from ref. (33)).

Field	R_2	R_2'
1.5	16.4 ± 1.6	65.4 ± 11.2
4.0	19.2 ± 3.4	178.4 ± 37.6

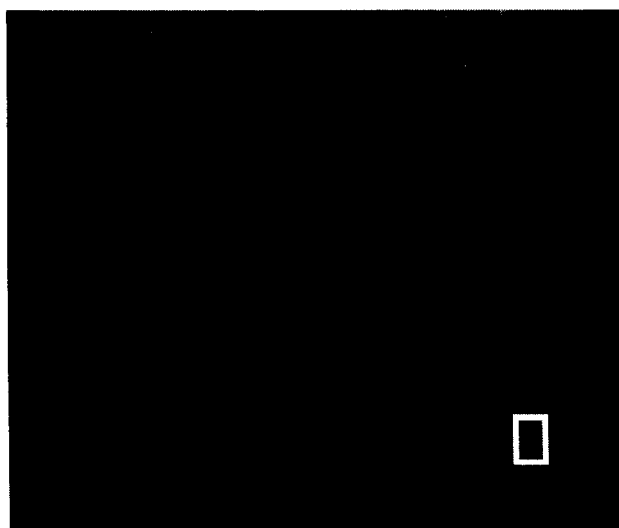
Measurement of Transverse Relaxation Rates

Although the quantity of interest is R_2 , the reversible contribution to the effective transverse relaxation rate, R_2 , much of the previous work has concentrated on the measurement of R_2' . Whereas an image-based measurement of R_2 , in general, is straightforward, the chemical heterogeneity of bone marrow is a complicating factor. Bone marrow has cellular (hematopoietic) and fatty component, with the relative fractions varying widely depending on anatomic site and age. A line width measurement by means of image-guided localized spectroscopy has the advantage of providing T_2 for each spectral component (35). However, image-based (non spectrally resolved) techniques are generally preferred since they allow for retrospective selection of a region of interest (ROI), either by means of gradient echo (35–37) or asymmetric spin-echo techniques (38, 39). The information of the two methods differs somewhat in that the gradient echo signal amplitude decays with a rate constant R_2 , whereas the asymmetric spin echo evolves with R_2' . By collecting an array of images with incrementally stepped time for inhomogeneity dephasing (gradient echo delay or echo offset), the pixel amplitudes can be fitted to some model for signal decay. In terms of efficiency, the gradient echo is preferable since multiple time points can be sampled from a single train of echoes (40, 41) whereas the echo offset method requires individual acquisitions (unless they are concatenated in which case the scan time still scales with the number of echo offset time points (42)).

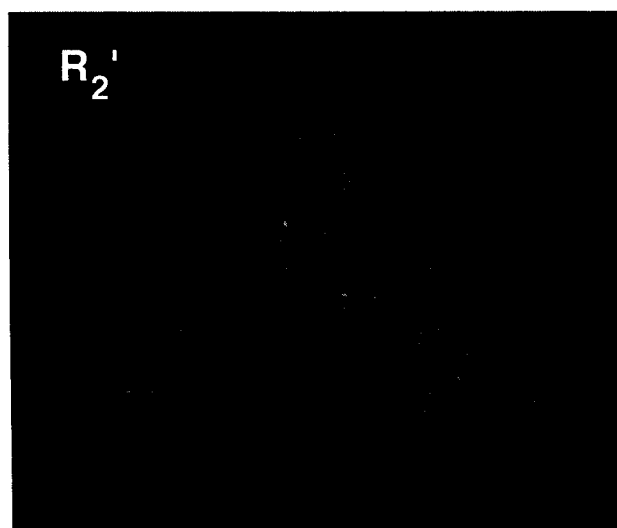
The presence of multiple chemically shifted constituents (water and fat with its various spectral components) causes an amplitude modulation which has the characteristics of an interferogram. The latter can be expressed as the modulus of the vector sum of the individual phase-modulated spectral components (36, 43). Typically, the most abundant spectral components are those of the CH_2 protons of fatty acids and of water which are separated by $\delta = 3.35$ ppm. It has been shown that the amplitudes can be fitted to a two-component interferogram with T_2 , fat and water signal amplitudes as adjustable parameters and assuming $T_{2, \text{fat}} \approx T_{2, \text{water}}$ (36). Multi-parameter

curve fits are hampered by the difficulty of locating the global minimum and require a relatively large number of images. One alternative is to suppress one spectral component (39), which sacrifices some and is relatively sensitive to global magnetic field inhomogeneity, demanding that the field across the sample volume vary less than the chemical shift. Another approach to suppress the modulation is to sample the interferogram at the modulation frequency, ideally in such a manner that the two components are in phase with one another (44). This condition is satisfied for sampling at multiples of the modulation period $T=(2\pi/\gamma \delta H_0)$ which is 4.65 ms at 1.5 T field strength.

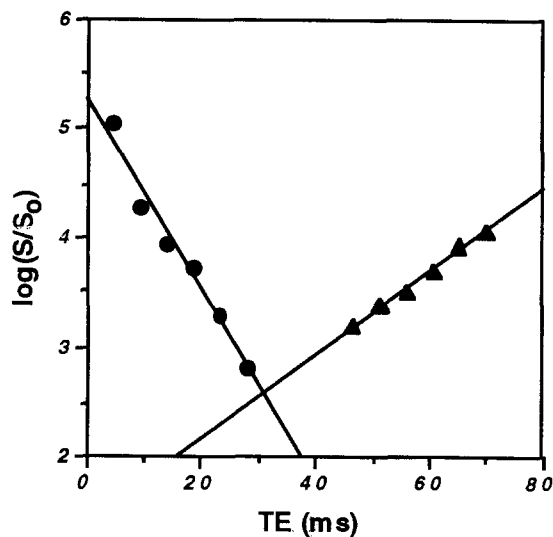
Recently, Ma and Wehrli reported a new multi-slice pulse sequence capable of measuring both the reversible and irreversible contribution to the transverse relaxation rate ($R_{2'}$ and R_2) in a single scan (34). The method, termed GESFIDE (gradient echo sampling of FID and echo) is based on sampling the descending and ascending portion of a Hahn echo with a train of gradient echoes. The transient signal before and after the phase-reversal RF pulse decays with rate constants $R_{2+} = R_2 + R_{2'}$ and $R_{2-} = R_2 - R_{2'}$, respectively. If, further, the time interval between successive gradient echoes is set equal to the fat-water chemical shift modulation period (see above), R_{2+} and R_{2-} can be determined by curve fitting and R_2 and $R_{2'}$ determined algebraically. Salient features of the method are its insensitivity to RF pulse imperfections, as well as its high precision and efficiency. Figs. 2a and b show an acquired GESFIDE image along with a computed $R_{2'}$ parameter image.



(a)



(b)



(c)

Figure 2. (a) First of a series of GESFIDE images used to compute the R_2 parameter map (b). Note the high intensity in the latter for structures pertaining to trabecular bone, consistent with enhanced R_2 due to susceptibility-induced line broadening. (c) Evolution of the gradient-echo signal from ROI in the greater trochanter (Fig. a). Prior to the phase-reversal pulse the signal evolves with a time constant $R_{2\cdot} = R_2 + R_{2'}$. The change in the sign of the slope indicates that $R_{2'} \gg R_2$ (from Ma and Wehrli (34), modified).

The susceptibility-induced line broadening depends on the dimensions of the volume element across which the inhomogeneity is measured. In an image-based measurement the smallest signal producing volume element is the imaging voxel. If the voxel size decreases below the order of magnitude of the intertrabecular space, then the likelihood for this voxel to fall into a region sufficiently removed from the field gradients induced by trabeculae, increases. As a consequence the mean T_2 histogram becomes wider and more asymmetric with decreasing pixel size. On the other hand, if the voxel size is large relative to the range of the gradients, T_2' becomes independent of voxel size, which is the case for pixels on the order of 1.5–2 mm.

High-Resolution Imaging of Trabecular Structure

Whereas the measurement of the induced magnetic field inhomogeneity provides structural information indirectly, high-resolution MRI at microscopic dimensions has the potential for nondestructive mapping of three-dimensional trabecular morphology, as an alternative to conventional microscopy from sections (45, 46). In fact, bone is ideal in that it has nearly background intensity, which facilitates image segmentation into bone and marrow. In order to measure the histomorphometric parameters such as trabecular volume fraction, mean thickness and

intertrabecular spacing, adequate resolution is required in the three spatial dimensions. Partial volume blurring ensues whenever the voxel size is on the order or larger than the structures to be visualized. In order to classify the image pixels into bone and bone marrow, a segmentation threshold is usually set. Whereas in an ideal image of trabecular bone the voxel intensity histogram consists of two delta functions, the presence of partial volume mixing and noise causes histogram broadening, and classification of the image pixels into bone and bone marrow becomes ambiguous. Chung et al. (47) have recently evaluated the technical requirements for microimaging at 9.4T and found the most critical data acquisition parameters to be (i) slice thickness, (ii) in-plane pixel size, and (iii) signal-to-noise ratio. Whereas lower limits for any of the parameters are difficult to establish, the following were found to provide for safe margins: a slice thickness of 200 μm or less, an in-plane pixel size on the order of 50 μm or less, and a SNR on the order of 5–10. Under these conditions the histogram was found to be bimodal and the choice of segmentation threshold uncritical.

Another problem that requires attention are the background gradients from the susceptibility-induced fields, which can cause artifacts in the form of signal loss from intravoxel phase dispersion (cf. eq.(1)). Since these phase losses are recoverable -- assuming diffusion to be negligible -- spin-echo detection is advantageous. Alternatively, the dephasing time should be held minimal which can, for example, be achieved with projection-reconstruction techniques, as they have been applied in micro imaging of lung parenchyma (48).

The potential use of NMR microscopy as a histologic tool for assessing age-related changes in trabecular morphology and their agreement with histology is implied by recent work in animal models (49). Since trabecular structure is anisotropic, three-dimensional (3D) imaging is advantageous as it permits display and thus analysis in all three orthogonal planes. An example of such an application illustrating highly anisotropic trabecular bone is displayed in Fig. 3, along with a 3D shaded surface display. From data like the ones shown, the fabric tensor can be determined by measuring the mean intercept lengths between trabeculae in all spatial directions.

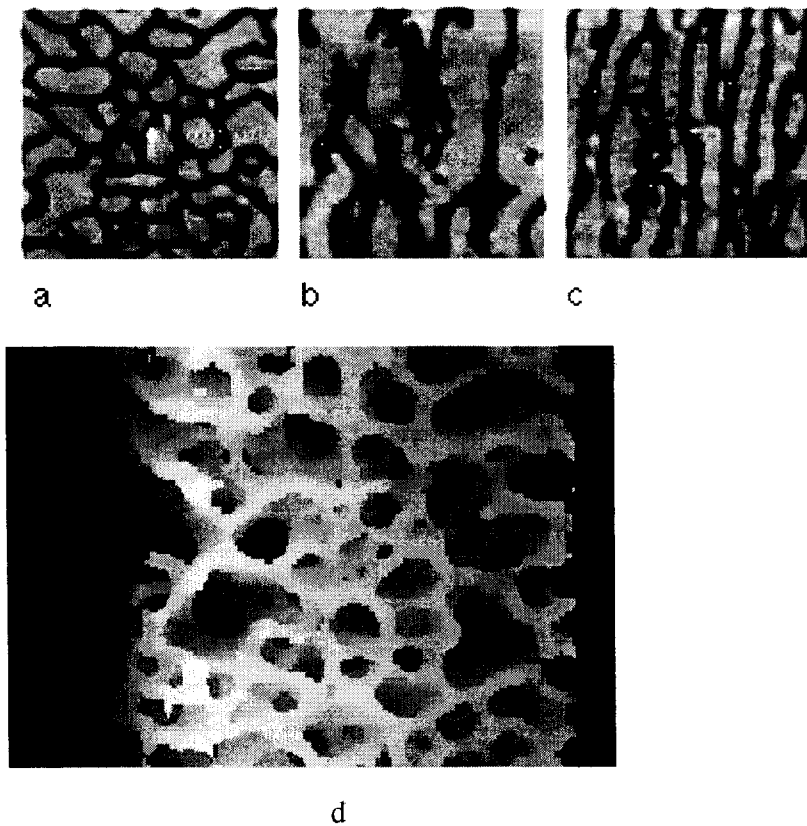


Figure 3. Images at microscopic dimension showing trabecular structure: (a)–(c) Orthogonal views obtained from 643 array of 3D spin-echo array of images acquired at 9.4T on a specimen of trabecular bone from bovine tibia ($114 \times 114 \times 139 \mu\text{m}^3$ voxel size); (a) transverse. (b), (c) longitudinal sections. Note preferential orientation of the trabeculae along inferior–superior direction. (d) Shaded surface display of same array of data, resolution-enhanced by means of a subvoxel tissue classification technique using Bayesian segmentation (50).

In our laboratory we have concentrated on a 3D embodiment of a partial flip-angle method (51) originally dubbed "RASEE" (rapid spin-echo excitation)) (52). RASEE permits operation at short TR with minimal saturation analogous to the gradient echo. The method is based on the idea of restoring the partially inverted magnetization in a $(\alpha - \tau - 180^\circ)$ pulse sequence with $\alpha > 180^\circ$. A salient feature of RASEE is the use of a composite pulse to circumvent the difficulty of engendering a selective pulse of flip angle greater than 90° . This pulse consists of a non-selective 180° pulse followed immediately by a slice-selective pulse of flip angle β in such a manner that the condition $\alpha = 180^\circ - \beta$ holds. Using this method Jara et al. were able to obtain images comparable to those in Fig. 3 in vivo in the finger.

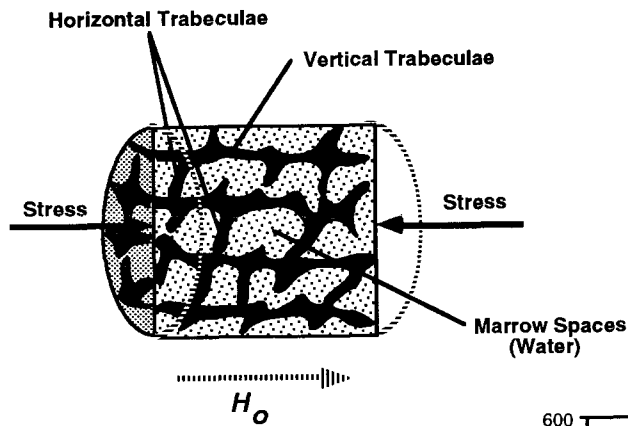
A significant improvement was FLASE (fast large-angle spin-echo) by Ma et al. (53) which combines the two pulses (non-selective 180° and selective α pulse) into a single Shinnar-LeRoux pulse. Along with other improvements such as splitting of the phase and slice-encoding pulses for very short echo times, we were able to obtain high-resolution images of trabecular structure in the wrist in vivo in patients with osteoporosis and control subjects.

Relationship between Trabecular Architecture and Mechanical Competence

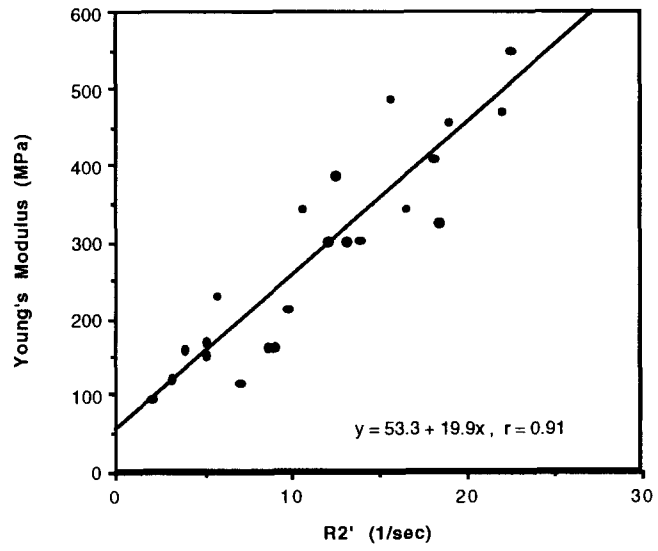
We have previously seen that trabecular bone is anisotropic with the orientation of the trabeculae following the major stress lines. In the vertebrae, for example, the preferred orientation of the trabeculae is along the body axis in response to the compressive forces acting in this direction. The role of the horizontal trabeculae is to act as cross ties preventing failure by buckling. It has been shown that during aging horizontal trabeculae are lost preferentially (54).

We shall now return to R_2' which we have seen to be closely related to the density and orientation of the trabeculae (see, for example eq. (5)). Therefore, if the static magnetic field is applied parallel to the inferior-superior axis of the vertebrae, the horizontal trabeculae (i.e. those orthogonal to the field) are polarized and thus are expected to be the principal cause of the susceptibility-induced line broadening. Chung et al (55) measured the mean spacing of horizontal trabeculae (i.e. the reciprocal of horizontal trabecular number density) in cadaver specimens of human lumbar trabecular bone after bone marrow removal and suspension of the bone in water, using NMR microscopy and digital image processing. They found a positive correlation between water proton R_2' , measured at 1.5 T and mean number density of the horizontal trabeculae ($r=0.74$, $p<0.0001$).

The critical role of the horizontal trabeculae in the vertebrae in conferring compressive strength is illustrated with the correlation between R_2 measured with the polarizing field parallel to the body axis and Young's modulus of elasticity (stiffness) for compressive loading. **Fig. 4a** shows the relationship between anatomic axis, trabecular orientation, the orientation of the applied magnetic field and the direction of compressive loading. A strong association between stiffness and R_2 exists over a wide range of values, corresponding to trabecular bone of very different morphologic composition (**Fig. 4b**). From these data it is inferred that a global measurement of R_2 in trabecular bone seems able to predict the compressive strength of this highly complicated structure.



a)



b)

Figure 4. (a) Cross section through cylindrical trabecular bone specimen (schematic) used for R_2' , structural and stress analysis. Cylinder axis is parallel to the anatomic inferior–superior axis, aligned with the external field polarizing predominantly horizontal trabeculae which cause line broadening of the proton resonances in the marrow spaces. Compressive loading is applied along cylinder axis. (b) Young's modulus of elasticity (in Megapascal, MPa) obtained from compression tests in 22 cylindrical specimens from the lumbar vertebral bodies of 16 human subjects aged 24 to 86 years human lumbar vertebrae, plotted as a function of R_2' the water protons in the intertrabecular spaces ($r=0.91$, $p<0.0001$). (From ref. (55), modified).

Hwang et al. (56) recently conceived a host of new structural parameters which can be derived at image resolutions and which they demonstrated to be able to predict Young's modulus in trabecular bone of the human radius. The method is based on probabilities for the occurrence of bone in one or multiple spatially related imaging voxels. The probability for bone to be present at some arbitrary location within the voxel is equal to the bone volume fraction (BVF). Since $BVF=1-MVF$ (marrow volume fraction) and MVF is proportional to the voxel intensity, MVF can readily

be determined provided the signal intensity of pure marrow is known. There was a fair correlation between Young's modulus for loading along the bone's axial direction ($R^2=0.57$, $p<0.00005$). However, this result leaves 43 % of the elastic modulus unexplained. The images in Figure 5 illustrate the fallacy of relying entirely on bone volume fraction while ignoring structure in that the specimen with the highest BVF is actually weakest! A cursory inspection of this specimen shows that the trabeculae are far less oriented in the direction of loading. These qualitative observations can be expressed in terms of several new parameters which rest on the concept of probabilities for the spatial distribution of the bone.

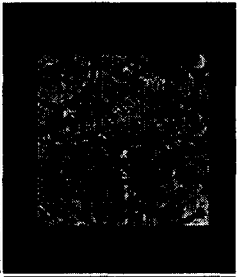
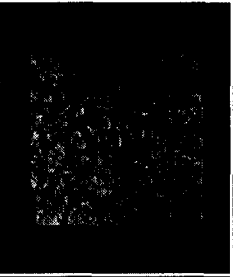
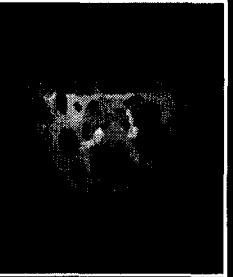
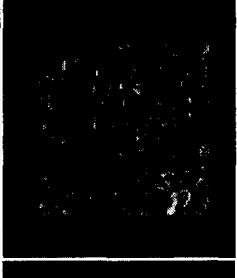
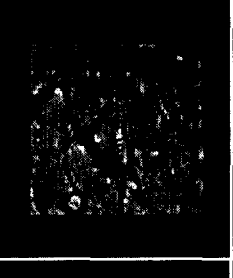

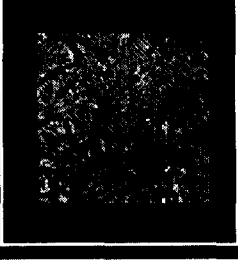
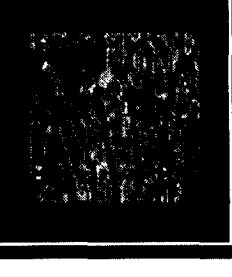
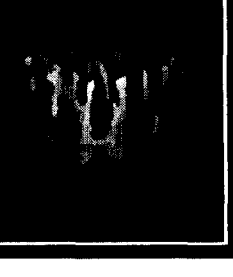
	BVF	YM (MPa)	Tansverse Section	Longitudinal Section	3D Projection
Specimen 1	0.16	316			
Specimen 2 ^a	0.14	676			
Specimen 3	0.12	543			

Figure 5. The variety of structures encountered in trabecular bone is exemplified by the cross-sectional and 3D projection NMR images of specimens from a 76-year-old man (specimen 1), an 80-year-old man (specimen 2), and a 53-year-old woman (specimen 3). Images were obtained in a 3D partial flip-angle spin-echo mode at a voxel size of $78 \times 78 \times 78 \mu\text{m}^3$ from cylindrical cores of 9 mm length and diameter. Note that in spite of specimen 1 having the highest BVF, it has the lowest modulus (from Hwang et al. (56)).

The probability that one point in a voxel and one point in a neighboring voxel are both in bone is equal to the product of the BVF's of the two voxels. In general, the two-point probabilities for all pairs of voxels with a given spatial offset can be averaged, resulting in the autocorrelation function (ACF) which has previously been used to characterize porous materials (57, 58):

$$ACF(n_x, n_y, n_z) = \langle P_1(x, y, z) P_1(x+n_x, y+n_y, z+n_z) \rangle_{x, y, z} \quad (6)$$

In eq. (6), $n_{x,y,z}$ are the voxel offsets in 3D space and the brackets, $\langle \rangle$, indicate a spatial average over all possible voxel locations (x, y, z) .

As implied by the images of Fig. 5, trabecular structure in the distal radius is highly anisotropic. However, since it is approximately transversely isotropic, the structure is adequately characterized by parameters which are averages in the transverse plane (perpendicular to the forearm) and by parameters which are measure in the longitudinal direction. A one-dimensional ACF can be computed for a transverse section as an angular average. The concept of two-point probabilities as quantities describing the spatial arrangement of the bone, is illustrated in Fig. 6.

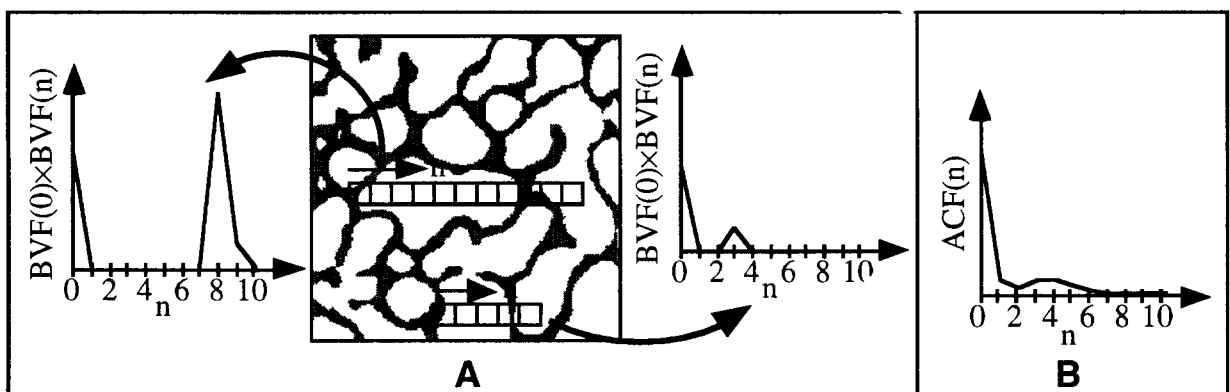


Figure 6. (A) The plots show the two-point probabilities for the two rows of voxels superimposed on the trabecular bone structure. (B) The ACF is the average of the two-point probabilities of all pairs of voxels with a given offset. The distance between the peak in the plot correspond to the distance between trabeculae.

The distance to the second peak is a measure of the averaged spacing of the trabeculae in the transverse plane, which is another commonly measured parameter for predicting bone quality

(59–62). To characterize an entire volume, the transverse spacing is averaged over all transverse sections. Similarly, the longitudinal spacing can be measured as the distance to the second peak in the autocorrelation in the z direction:

$$ACF_{\text{longitudinal}}(n_z) = ACF(0, 0, n_z) = \langle P_1(x, y, z)P_1(x, y, z+n_z) \rangle_{x,y,z} \quad (7)$$

The transverse contiguity (TCon) can be defined as the ratio of two-point probabilities:

$$TCon = ACF_{\text{transverse}}(1) / ACF_{\text{transverse}}(0) \quad (8)$$

which can be approximated as the ratio of the probability that two points from nearest neighbor voxels in the transverse plane are both in bone over the probability that two points from the same voxel are in bone.

Finally, a parameter called tubularity (Tub), expresses the probability that two points from adjacent voxels in the longitudinal direction are both in bone, divided by the probability that two points from the same voxel are both in bone:

$$Tub = \frac{\langle BVF(x,y,z_1)BVF(x,y,z_2) \rangle_{x,y}}{ACF_{\text{transverse}}(0)} \quad (9)$$

where z_1 and z_2 refer to the locations of adjacent transverse sections. The denominator of Tub is the larger of the two values of $ACF_{\text{transverse}}(0)$ from the two transverse sections. An entire VOI is characterized by averaging Tub over all pairs of adjacent transverse sections. The parameter quantifies the degree to which trabeculae are oriented parallel to the direction of the applied force. It is noted in Fig. 5 that the specimen 3, while having the lowest BVF, has high tubularity which confers the relatively high strength to this bone in spite of its relatively low BVF.

While none of the individual parameters correlated significantly better with Young's modulus than BVF, the longitudinal spacing, tubularity and BVF together were found to predict 91 % of the 23 specimens' elastic modulus. These results emphasize the importance of architecture in conferring strength to the trabecular bone and illustrate why bone mineral density (the counterpart of the measured BVF) is a poor predictor of fractures.

Empirical Relationship with Bone Mineral Density

The early work by Ford and Wehrli (35) suggests a possible relationship between bone mineral density and the extent of inhomogeneity broadening measured by T_2^* . They found T_2^* in the distal femur to shorten with increasing density of trabeculation from the diaphysis (lowest trabeculation) toward the metaphysis and epiphysis of the bone (highest trabeculation), an observation first made qualitatively by Sebag and Moore (63). Majumdar et al (37) determined R_2' in intact specimens of human vertebral trabecular bone after bone marrow removal and suspending the bone in saline. The measurements afforded a linear correlation between R_2' and bone mineral density (in mgcm^{-3}), obtained from quantitative computed tomography (QCT), with a slope of $0.20 \pm 0.02 \text{ s}^{-1}\text{mg}^{-1}\text{cm}^3$ ($r^2=0.85$). More recently, the same group extended these studies in vivo in normal volunteers to the distal radius and proximal tibia (39). Confirming earlier work they found both bone mineral density and R_2' to be dependent on the anatomic site of measurement. In excellent agreement with in vitro data they measured $0.20 \pm 0.01 \text{ s}^{-1}\text{mg}^{-1}\text{cm}^3$ ($r=0.88$) for the combined data from both anatomic sites.

Clinical Studies in Patients with Osteoporosis

An early pilot study on a small group of patients with clinically established osteoporosis of the spine ($n=12$) and an equal number of control subjects, showed the former to have significantly reduced bone marrow R_2^* in lumbar vertebra L5 (36). More recently, Sugimoto et al (64) showed in 15 subjects (6 normal volunteers and 9 post-oophorectomy patients, that the latter had reduced R_2^* (17.4 vs. 14.3 ms), measured at 1.5T field strength. Funke et al. (41), using similar methodology, obtained good discrimination, expressed in terms of R_2^* , in a group of 20 osteoporotics and 48 control subjects. Patients, however, were merely characterized as having 'reduced lumbar bone density' on DEXA or QCT, without providing cut-off criteria. Further, there was a substantial age disparity in the two populations, which was not corrected for. Nevertheless, these investigators' results are encouraging, indicating that with improvements in measurement methodology, excellent diagnostic accuracy should be possible.

The largest study today is the one by Wehrli et al. (65) comprising 145 postmenopausal women. The control population ($n=77$, mean age 46.6 ± 14.9 years) consisted of women with mean spinal bone mineral densities (BMD) $> 0.9 \text{ g/cm}^2$ (DEXA) or $> 90 \text{ mg/cm}^3$ (QCT), and no vertebral deformities; the patient population ($n=59$, mean age 59.7 ± 10.2 years) of women with osteoporosis of the spine, exhibiting at least one radiographic deformity of the thoracic vertebrae

and/or BMD below the cutoff for controls. The extent of deformity was also determined as a mean deformity index, DI_{av} . This study was designed to explore whether image-based measurements of T_2^* may provide an index of the integrity of trabecular bone as a possible criterion for predicting fracture risk.

R_{2^*} was significantly lower in osteoporotics for all L vertebrae ($p < 0.001$), except for L1. The best discriminator was the average of L3–L5 ($R_{2^*_{av}}$) for which means and standard errors obtained were $64.79 \pm 1.18 \text{ s}^{-1}$ and $53.39 \pm 1.24 \text{ s}^{-1}$ in controls and osteoporotics, respectively ($p < 0.0001$). R_{2^*} decreased with age in control subjects by ca. $3 \text{ s}^{-1}/\text{decade}$ ($r = 0.42$, $p < 0.005$) or $9 \text{ s}^{-1}/\text{decade}$ in postmenopausal. After age correction accounting for the different ages of the two populations, discrimination in terms of $R_{2^*_{av}}$ was reduced (64.78 ± 1.07 and $57.22 \pm 1.17 \text{ s}^{-1}$, $p < 0.0001$). In a subset of 38 age-matched pairs of osteoporotics and controls the difference $\Delta R_{2^*_{av}} = R_{2^*_{control}} - R_{2^*_{osteo}}$ was $+8.25 \pm 10.40 \text{ s}^{-1}$ for the average of L3–L5 ($p < 0.0001$). Diagnostic accuracy, expressed in terms of the area under the ROC curve, was 80 % and 72 %, without and with age correction, respectively. Based on binary decision criteria for presence of deformities, subjects with deformities had lower $R_{2^*_{av}}$ than controls (52.3 ± 1.6 vs. $62.5 \pm 1.1 \text{ s}^{-1}$, $p < 0.0001$), but the discrimination was better for mean vertebral DEXA BMD ($p < 0.0001$). Both R_{2^*} and BMD correlated with DI_{av} , the correlation with R_{2^*} being slightly stronger ($r = 0.40$, $p < 0.0005$, vs. $r = 0.36$, $p < 0.0001$). $R_{2^*_{av}}$ was significantly correlated with mean BMD ($r = 0.54$, $p < 0.0001$, slope = $31.4 \text{ s}^{-1}/\text{gcm}^{-2}$, $p < 0.0001$).

In a very recent study by Grampp et al. (66), involving a small number of healthy pre- and postmenopausal women (groups I and II), as well as women with spinal fractures (group III), R_{2^*} in the distal radius correlated well with QCT BMD, but not with total (DEXA) BMD. Interestingly, R_{2^*} was the only technique to distinguish groups I and II but was unable to distinguish between groups II and III. The number of subjects studied, however, was small, hence these results should be regarded with some caution.

While too early to predict the effectiveness of quantitative MRI as a diagnostic and prognostic criterion, the method has potential for screening of the population at risk, mainly women before and after menopause, with hereditary or lifestyle-related risk factors. This would represent a new application of MRI, differing fundamentally from its current widespread diagnostic use. Whether such a scenario will materialize depends, besides effectiveness relative to established procedures, on procedure and equipment cost.

References

1. J. Wolff. *Das Gesetz der Transformation der Knochen* (A. Hirschwald, Berlin. 1892).
2. B. Riggs and L. Melton. *Osteoporosis* (Raven Press, New York, 1988).
3. D. M. Reid, J. J. Nicoll, N. Brown, M. A. Smith, P. Tothill, and G. Nuki. Bone mass in corticosteroid treated patients with rheumatoid arthritis, asthma and polymyalgia rheumatica. *Scott Med J* **30**, 54 (1985).
4. P. Ruegsegger, T. C. Medici, and M. Anliker. Corticosteroid-induced bone loss. A longitudinal study of alternate day therapy in patients with bronchial asthma using quantitative computed tomography. *Eur J Clin Pharmacol* **25**, 615 (1983).
5. C. E. Brown, J. R. Allaway, K. L. Brown, and H. Battocletti. Noninvasive evaluation of mineral content of bone without the use of ionizing radiation. *Clin Chem* **33**, 227 (1987).
6. J. Ackerman, D. Raleigh, and M. Glimcher. Phosphorus-31 magnetic resonance imaging of hydroxyapatite: a model for bone imaging. *Magn Res Medicine* **25**, 1 (1992).
7. J. Moore, L. Garrido, and J. Ackerman. Solid-state ³¹P magnetic resonance imaging of bone mineral. *Magn Reson Medicine* **33**, 293 (1995).
8. Y. Wu, M. Glimcher, C. Rey, and J. Ackerman. A unique protonated phosphate group in bone mineral not present in synthetic calcium phosphates. Identification by phosphorus-31 solid state NMR spectroscopy. *J Mol Biol* **244**, 423 (1994).
9. J. Glasel and K. Lee. On the interpretation of water nuclear magnetic resonance relaxation times in heterogeneous systems. *J Am Chem Soc* **96**, 970 (1974).
10. C. A. Davis, H. K. Genant, and J. S. Dunham. The effects of bone on proton NMR relaxation times of surrounding liquids. *Invest Radiol* **21**, 472 (1986).
11. D. C. Ailion, T. A. Case, D. Blatter, A. H. Morris, A. Cutillo, C. H. Durney, and S. A. Johnson. Applications of NMR spin imaging to the study of lungs. *Bull Magn Res* **6**, 130 (1984).
12. K. K. Kwong, J. W. Belliveau, D. A. Chesler, I. Goldberg, R. Weisskoff, B. Poncelet, D. Kennedy, B. Hoppel, M. Cohen, R. Turner, H. Cheng, T. Brady, and B. Rosen. Dynamic magnetic resonance imaging of human brain activity during primary sensory stimulation. *Proc Natl Acad Sci* **89**, 5675 (1992).
13. S. Ogawa, D. W. Tank, R. Menon, J. M. Ellerman, K. Seong-Gi, H. Merkle, and K. Ugurbil. Intrinsic signal changes accompanying sensory stimulation: functional brain mapping with magnetic resonance imaging. *Proc Natl Acad Sci* **89**, 5951 (1992).
14. D. A. Yablonskiy and E. M. Haacke, Theory of NMR signal behavior in magnetically

- homogeneous tissues: the static dephasing regime. *Magn Reson Medicine* **32**, 749 (1994).
15. D. A. Yablonskiy, W. R. Reinus, and E. M. Haacke, Effect of anisotropic relaxation on bone mineral density measurement, Proc Int Soc Magn Reson Medicine, Third Annual Meeting New York, 1996, vol. 2, pp. 869.
 16. D. Newitt, S. Majumdar, M. D. Jergas, S. Grampp, and H. K. Genant, Decay characteristics of bone marrow in the presence of a trabecular bone network: In vitro and in vivo studies showing a departure from monoexponential behavior. *Magn Reson Medicine* **35**, in press (1996).
 17. J. C. Ford, F. W. Wehrli, and H. Chung, Magnetic field distribution in models of trabecular bone. *Magn Reson Medicine* **29**, 373 (1993).
 18. T. S. Sumanaweera, G. H. Glover, T. O. Binford, and J. R. Adler, MR susceptibility misregistration correction. *IEEE Trans Med Imag* **12**, 251 (1993).
 19. S. N. Hwang, F. W. Wehrli, and H. C. Chung, Experimental evaluation of theoretical field maps in human trabecular bone, Proc Int Soc Magn Reson Medicine, Third Annual Meeting. New York, 1996, vol. 2, pp. 1371.
 20. H. Chung, S. N. Hwang, H. N. Yeung, and F. W. Wehrli, Mapping of the magnetic field distribution in cancellous bone. *J Magn Reson Ser B* in press, (1996).
 21. F. Wehrli and S. Wehrli, A Novel Approach toward Measurement of the Diamagnetic Susceptibility of Bone, Proc Soc Magn Res Medicine, 10th Annual Meeting San Francisco, (1991), vol. 1, pp. 250.
 22. J. A. Hopkins and F. W. Wehrli, Magnetic susceptibility measurement of insoluble solids by NMR: magnetic susceptibility of bone. *Magn Reson Medicine* in press, (1996).
 23. P. C. Lauterbur, B. V. Kaufman, and M. K. Crawford, in *Biomolecular Structure and Function* (Academic Press, New York, 1978) pp. 329.
 24. A. Morrish, *The Physical Principles of Magnetism* (Robert E. Krieger Publishing Co., Malabar, FL, 1983).
 25. L. J. Gibson, The Mechanical Behaviour of Cancellous Bone. *Journal of Biomechanics* **18**, 317 (1985).
 26. K. Engelke, S. Majumdar, and H. Genant, Phantom studies simulating the impact of trabecular structure on marrow relaxation time, T2 phantom studies. *Magn Reson Medicine* **31** 380 (1994).
 27. S. Hwang and F. Wehrli, The calculation of the susceptibility-induced magnetic field from 3d NMR images with applications to trabecular bone. *J Magn Reson Ser B* **109**, 126 (1995).
 28. H. Chung and F. W. Wehrli, T2' and material anisotropy of cancellous bone, Proc Soc Magn Reson Medicine, 12th Annual Meeting New York, 1993', vol. 1, pp. 138.

29. D. A. Yablonsky, W. R. Reinus, E. M. Haacke, and H. Stark, Quantitation of T2' anisotropic effects on MR bone mineral density measurement. *Magn. Reson. Medicine* **in press**, (1996).
30. K. Selby, S. Majumdar, D. C. Newitt, and H. K. Genant, Investigation of MR decay rates in microphantom models of trabecular bone. *J Magn Reson Imaging* **6**, 549 (1996).
31. P. Parizel, B. van Riet, B. van Hasselt, H. Dijkstra, L. van den Houwe, J. van Goethem, P. van Wiechen, and A. de Schepper, Influence of magnetic field strength on T2' decay and phase effects in gradient echo MRI of vertebral bone marrow. *J Comput Assist Tomogr* **19**, 465 (1995).
32. H. K. Song, F. W. Wehrli, and J. Ma, Field strength dependence of trabecular bone marrow transverse relaxation, Proc Int Soc Magn Reson Medicine New York, 1996, vol. 2, pp. 870
33. H. K. Song, F. W. Wehrli, and J. Ma, Field strength and angle dependence of trabecular bone marrow transverse relaxation in the calcaneus. *J. Magn Reson Imaging* **in press**, (1996).
34. J. Ma and F. W. Wehrli, Method for image-based measurement of the reversible and irreversible contribution to the transverse relaxation rate. *J Magn Reson Ser B* **111**, 61 (1996).
35. J. C. Ford and F. W. Wehrli, In-vivo quantitative characterization of trabecular bone by NMR interferometry and localized proton spectroscopy. *Magn Reson Medicine* **17**, 543 (1991).
36. F. W. Wehrli, J. C. Ford, M. Attie, H. Y. Kressel, and F. S. Kaplan, Trabecular structure: preliminary application of MR interferometry. *Radiol* **179**, 615 (1991).
37. S. Majumdar, D. Thomasson, A. Shimakawa, and H. K. Genant, Quantitation of the susceptibility difference between trabecular bone and marrow: experimental studies. *Magn Reson Medicine* **22**, 111 (1991).
38. G. Wismer, R. Buxton, B. Rosen, C. Fisel, R. Oot, T. Brady, and K. Davis, Susceptibility-induced MR line broadening: applications to brain iron mapping. *J Comput Assist Tomogr* **12**, 259 (1988).
39. S. Majumdar and H. K. Genant, In vivo relationship between marrow T2' and trabecular bone density determined with a chemical shift-selective asymmetric spin-echo sequence. *J Magn Reson Imaging* **2**, 209 (1992).
40. F. W. Wehrli, S. N. Hwang, J. C. Ford, and H. Jara, Method for Image-Based T2' Measurement in Bone Marrow, Proc Magn Res, 2nd Meeting 1994, vol. 1, pp. 201.
41. M. Funke, H. Bruhn, R. Vosschenrich, O. Rudolph, and E. Grabbe, Bestimmung der T2'-Relaxationszeit zur Charakterisierung des trabekularen Knochens. *Fortschr Geb Roentgenstr Neuen Bildgeb Verfahr* **161**, 58 (1994).
42. G. H. Glover, Multi-point Dixon technique for water and fat proton and susceptibility imaging. *J Magn Reson Imaging* **1**, 521 (1991).
43. F. W. Wehrli, D. G. Perkins, A. Shimakawa, and F. Roberts, Chemical shift-induced amplitude

- modulations in images obtained with gradient refocusing. *Magn Res Imaging* **5**, 157 (1987).
44. J. C. Ford and F. W. Wehrli, Alternative approach to measuring T2' in trabecular bone. *J Magn Res Imaging* **2(P)**, 103 (1992).
 45. A. M. Parfitt, in *Bone Histomorphometry: Techniques and Interpretation* R. R. Recker, Eds. (CRC Press, Boca Raton, FL, 1981) pp. 53.
 46. R. R. Recker, Eds., *Bone histomorphometry: techniques and interpretation* (CRC Press, Boca Raton, 1983).
 47. H. Chung, F. Wehrli, J. Williams, S. Kugelmass, and S. Wehrli, Imaging and quantitative analysis of trabecular microstructure by nuclear magnetic resonance microscopy. *J Bone Min Res* **10**, 803 (1995).
 48. S. Gewalt, G. Glover, L. Hedlund, G. Cofer, J. MacFall, and G. Johnson, MR microscopy of the rat lung using projection-reconstruction. *Magn Res Medicine* **29**, 99 (1993).
 49. R. D. Kapadia, W. B. High, H. A. Souleleveld, D. Bertolini, and S. K. Sarkar, Magnetic resonance microscopy in rat skeletal research. *Magn Res Medicine* **30**, 247 (1993).
 50. Z. Wu, H. Chung, and F. W. Wehrli, A Bayesian approach to subvoxel tissue classification in NMR microscopic images of trabecular bone. *Magn Res Medicine* **31**, 302 (1994).
 51. H. Jara, F. W. Wehrli, and H. Chung, High-resolution variable flip angle 3D MR imaging of trabecular microstructure in vivo. *Magn Res Medicine* **29**, 528 (1993).
 52. A. R. Bogdan and P. M. Joseph, RASEE: a rapid spin-echo pulse sequence. *Magn Res Imaging* **8**, 13 (1990).
 53. J. Ma, F. Wehrli, and H. Song, Fast 3D large-angle spin-echo imaging (3D FLASE). *Magn Reson Medicine* **35**, 903 (1996).
 54. L. Mosekilde and L. Mosekilde, Sex differences in age-related changes in vertebral body size, density and biomechanical competence in normal individuals. *Bone* **11**, 67 (1990).
 55. H. Chung, F. W. Wehrli, J. L. Williams, and S. D. Kugelmass, Relationship between NMR transverse relaxation, trabecular bone architecture and strength. *Proc. Natl Acad. Sci* **90**, 10250 (1993).
 56. S. N. Hwang, F. W. Wehrli, and J. L. Williams, Probability-based structural parameters from 3D NMR images as predictors of trabecular bone strength. *Proc. Natl Acad. Sci.* submitted, (1996).
 57. J. G. Berryman, Measurement of spatial correlation functions using image processing techniques. *J Appl Phys* **57**, 2374 (1985).
 58. G. Barrall, L. Frydman, and G. Chingas, NMR diffraction and spatial statistics of stationary systems. *Science* **255**, 714 (1992).
 59. L. Mosekilde, Sex differences in age-related loss of vertebral trabecular bone mass and

structure--biomechanical consequences. *Bone* **10**, 425 (1989).

60. A. M. Parfitt, C. H. E. Mathews, A. R. Villanueva, M. Kleerekoper, B. Frame, and D. S. Rao, Relationship between surface, volume, and thickness of iliac trabecular bone in aging and in osteoporosis. *J Clin Invest* **72**, 1396 (1983).
61. S. A. Goldstein, R. Goulet, and D. McCubbrey, Measurement and significance of three-dimensional architecture to the mechanical integrity of trabecular bone. *Calcif Tissue Int* **53**, S127 (1993).
62. B. D. Snyder, S. Piazza, W. T. Edwards, and W. C. Hayes, Role of Trabecular Morphology in the Etiology of Age-Related Vertebral Fractures. *Calcified Tissue International* **53**, S14 (1993).
63. G. H. Sebag and S. G. Moore, Effect of trabecular bone on the appearance of marrow in gradient-echo imaging of the appendicular skeleton. *Radiol* **174**, 855 (1990).
64. H. Sugimoto, T. Kimura, and T. Ohsawa, Susceptibility effects of bone trabeculae. Quantification in vivo using an asymmetric spin-echo technique. *Invest Radiol* **28**, 208 (1993).
65. F. W. Wehrli, J. C. Ford, and J. G. Haddad, Osteoporosis: clinical assessment with quantitative magnetic resonance imaging in diagnosis. *Radiol* **196**, 631 (1995).
66. S. Grampp, S. Majumdar, M. Jergas, D. Newitt, P. Lang, and H. K. Genant, Distal radius: in vivo assessment with quantitative MR imaging, peripheral quantitative CT, and dual X-ray absorptiometry. *Radiol* **198**, 213 (1996).